

New edge detection methods for seismic interpretation

Brian Russell¹ and Claude Ribordy¹

¹ Hampson-Russell, A CGG Company, Calgary, Alberta, brian.russell@cgg.com

ABSTRACT

In this article, we will discuss a new set of edge detection methods for seismic interpretation that involve derivatives of the seismic volume in the time, inline and cross-line directions. The methods discussed in this paper were adapted from techniques that were initially applied to potential field data for edge enhancement. These methods are similar to algorithms that have already been proposed for seismic edge detection, which involve spatial differences between traces. However, the difference between these new approaches and the original methods is the way in which the vertical derivative is introduced into the computation. The edge detection methods discussed here are also similar to coherency and semblance-based methods for seismic discontinuity detection, which in their initial form were based on cross-correlations between traces rather than derivatives. However, we can show that coherency estimates can also be implemented using temporal and spatial instantaneous attributes, which in turn depend on derivatives of the seismic trace and its Hilbert transform in the time, inline and cross-line directions. Since these methods require differentiation, products and differences of two separate seismic volumes (the original volume and its Hilbert transform) the potential for numerical instability is greater. The methods discussed in this article will be illustrated by a structurally complex seismic volume recorded in the North Sea.

INTRODUCTION

The first discussion of edge detection in the seismic literature was by Luo et al. (1996) in which they use differences between seismic traces to perform edge detection. This was a simple and effective method that produced good results which highlighted the discontinuities present on a seismic volume. By taking the differences between seismic traces, Luo et al. (1996) were performing a first-order spatial derivative operation, in which the data is convolved with a simple two or three point filter given as (-1,1) for the two trace case or (-1,0,1) for the three trace case. The latter option is called the centered difference operator. As pointed out by al-Dossary et al. (2006), this simple form of the filter has problems with sharp edges and noisy data. They propose the use of either the Canny (1986) filter, which is based on a 2D Gaussian function and its first and second derivatives, or a filter based on Green's function which was proposed by Torreao and Amaral (2002). The mathematical details of these filters are given by al-Dossary et al. (2006), and Figure 1, taken from that paper, shows the results of each filter. Based on the results shown in Figure 1, we felt justified in using the simple 3-point derivative filter for the implementations of the methods discussed in this article.

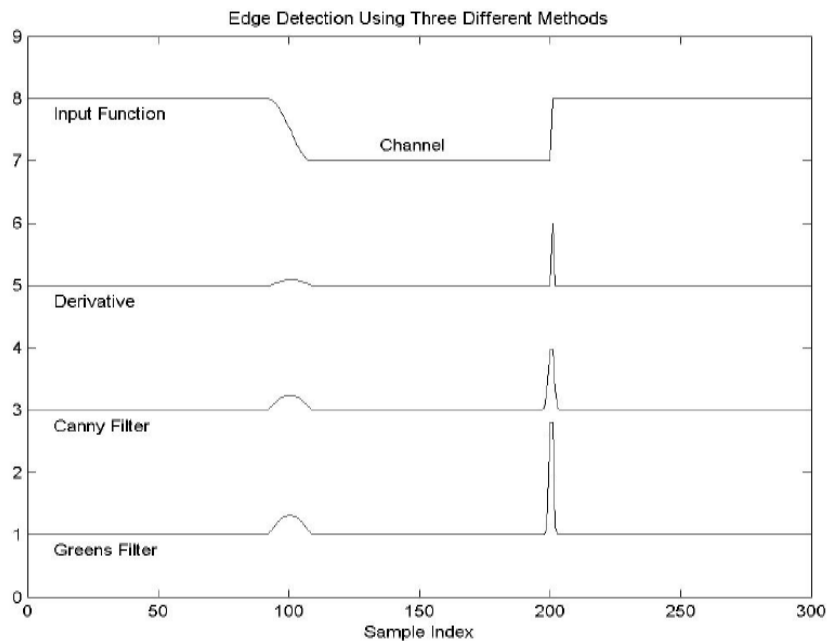


Figure 1. Comparison of three different edge detection algorithms (from al-Dossary et al., 2006).

More recently, a number of coherency and semblance-based methods have been developed for seismic discontinuity analysis, which in their initial form were based on cross-correlations between traces rather than derivatives (Bahorich and Farmer, 1995, Marfurt et al., 1998, Gersztenkorn and Marfurt, 1999). As we will show later, the results from these coherency algorithms are similar to the results from edge detection algorithms.

Often, when geophysicists think of attributes they first think of instantaneous attributes. In a previous CREWES talk (Russell, 2012) the first author discussed the influence of Dennis Gabor on the development of seismic attributes. His invention of the complex signal, using the Hilbert transform (Gabor, 1946), led to the concept of instantaneous amplitude, phase and frequency in the time domain, methods that were subsequently introduced into seismic processing by Taner et al. (1979). Luo et al. (1996) also discuss the application of their differencing method to the instantaneous phase and frequency attributes derived from a seismic volume.

Until recently it was not clear how instantaneous attributes were related to edge detection attributes. The link was developed by Barnes (1996) and al-Dossary and Marfurt (2006), who introduced the concept of instantaneous wavenumber in both the inline and cross-line directions of a seismic volume and showed how these attributes could be combined with temporal instantaneous frequency to produce estimates of dip and curvature, which are related to coherency. Since the instantaneous frequency and wavenumber involve combinations of the derivatives of both the seismic trace and its Hilbert transform, there is potential for instability when computing the seismic attributes. The edge detection methods for seismic interpretation discussed in this article involve only derivatives of the seismic trace in the time, inline and cross-line directions, thus reducing the algorithmic instability.

THE VERTICAL AND HORIZONTAL DERIVATIVE

To understand the effect of differentiating the seismic trace let us first consider a one-dimensional Gaussian shape which is given by the formula:

$$g(t) = A \exp\left(-\frac{t^2}{\sigma^2}\right), \quad (1)$$

where σ gives the width of the Gaussian and A gives its amplitude. The derivative of this function is

$$\frac{dg(t)}{dt} = -2A \frac{t}{\sigma^2} \exp\left(-\frac{t^2}{\sigma^2}\right). \quad (2)$$

These two functions are plotted in Figure 2 and it is clear from this plot that the derivative of the Gaussian function has an extra zero crossing and thus creates a discontinuity in the original function. That is, it turns peaks into edges. This can also be thought of as a “sharpening” function on a seismic pulse.

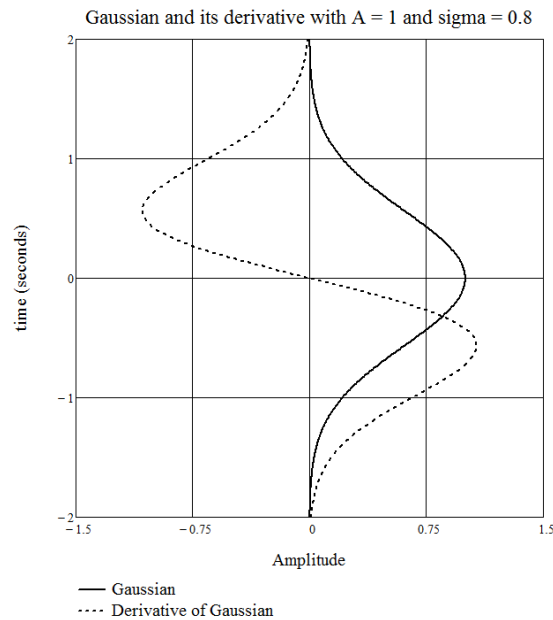


Figure 2: The Gaussian pulse (heavy line) and its derivative (dotted line) in the time direction.

Another way to look at the effect of the derivative on the seismic trace is to consider the effect of differentiation on a single frequency component given by $f(t) = \exp(i\omega t) = \cos(\omega t) + i \sin(\omega t)$, where $i = \sqrt{-1}$, $\omega = 2\pi f$ and f = frequency. The derivative of this function is given by

$$\frac{df(t)}{dt} = i\omega \exp(i\omega t). \quad (3)$$

Since i can be thought of as a 90 degree phase shift, differentiation increases the frequency content of the signal by multiplying the signal by the angular frequency term and rotates it by 90 degrees.

Since seismic data is a function of inline coordinate x and cross-line coordinate y in addition to vertical coordinate t , we should more formally use a partial derivative operator to define the vertical derivative, or $\frac{\partial f(x, y, t)}{\partial t}$. In a similar fashion we can define the partial derivative in the x direction as $\frac{\partial f(x, y, t)}{\partial x}$ and partial derivative in the y direction as $\frac{\partial f(x, y, t)}{\partial y}$. In the equations that follow in the next section, we simplify our notation by dropping the x , y , and t terms from the function f since they are implied by the partial differentiation. The inline and crossline derivatives can be illustrated by the same figure as before except that it has been rotated to show horizontal distance rather than vertical time, as shown in Figure 3.

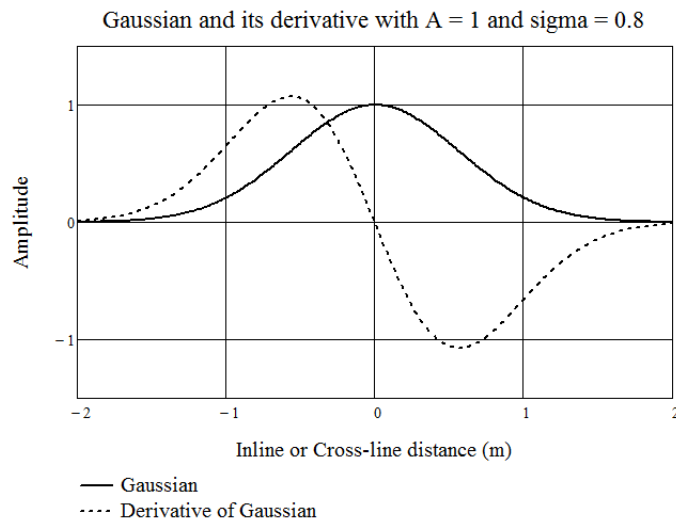


Figure 3: The Gaussian pulse (heavy line) and its derivative (dotted line) in the inline or cross-line direction.

As with the vertical, or time, derivative the spatial derivative also converts a peak to a zero-crossing, and thus enhanced any discontinuities found in the spatial x or y direction on the seismic data. We can also apply the frequency analysis of equation 3 to the spatial derivatives, which again tells us that differentiation in the horizontal direction increases the frequency content and applies a ninety degree phase shift. From these properties of the derivative in the time and horizontal directions and the temporal and spatial frequency domains, it appears reasonable that the derivative could be used to detect subtle changes in the seismic signal that relate to edges such as faults or fractures. It should also be noted that the Gaussian derivatives shown in Figures 2 and 3 were used by al-Dossary et al. (2006) in their implementation of the Canny filter.

EDGE DETECTION ATTRIBUTES

Cooper and Cowan (2008) review the potential field literature and summarize a number of algorithms for the edge enhancement of potential-field data that had been developed by previous authors. The authors also introduce their own new algorithm which is based on normalized statistics. Cooper and Cowan (2008) first remark that “a commonly used edge-detection filter is the total horizontal derivative (*TDX*)”, but do not supply a reference. They define *TDX* mathematically as

$$TDX = \sqrt{\left(\frac{\partial f}{\partial x}\right)^2 + \left(\frac{\partial f}{\partial y}\right)^2}. \quad (4)$$

Chopra and Marfurt (2012) call this filter the Laplacian and refer to its output as mean amplitude curvature, yet another attribute that is useful for estimating seismic discontinuities. The two dimensional filter *TDX* given equation 4 is also known as the Sobel filter and is used in image processing to sharpen photographic images. An excellent discussion of the Sobel filter for image enhancement is given by Gonzalez and Woods (2008). They point out that the two spatial derivatives found in equation 4 can be expressed as the gradient vector given by

$$\nabla f = \begin{bmatrix} \frac{\partial f}{\partial x} \\ \frac{\partial f}{\partial y} \end{bmatrix}. \quad (5)$$

Thus, the *TDX* operator in equation 4 is actually the magnitude, or length, of the gradient operator, which can be written mathematically as $|\nabla f|$ and is also referred to as the Laplacian (hence the terminology used by Chopra and Marfurt, 2012). The Sobel filter is actually the name given to the numerical implementation of the spatial derivatives on a 3 x 3 grid, as shown in Figure 4.

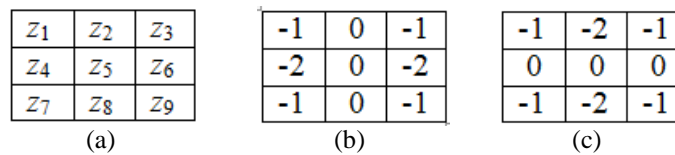


Figure 4: The numerical implementation of the Sobel filter, where (a) shows the 3 x 3 grid notation, (b) shows the weights used for the *x* derivative, and (c) shows the weights used for the *y* derivative, where *x* is the horizontal direction and *y* is the vertical direction.

Figure 4(a) explains the notation for the nine values in the 3 x 3 grid, Figure 4(b) shows the numerical implementation of the *x* derivative, and Figure 4(c) shows the numerical implementation of the *y* derivative, where *x* is the horizontal direction and *y* is the vertical direction.

This can be written mathematically as

$$\frac{\partial f}{\partial x} = (z_7 + z_8 + z_9) - (z_1 + z_2 + z_3), \quad (6)$$

and

$$\frac{\partial f}{\partial y} = (z_3 + z_6 + z_9) - (z_1 + z_4 + z_7). \quad (7)$$

Miller and Singh (1994) introduced the concept of the normalized vertical derivative, which they call the tilt angle, T , and which they express as

$$T = \arctan \left[\frac{\frac{\partial f}{\partial t}}{\sqrt{\left(\frac{\partial f}{\partial x}\right)^2 + \left(\frac{\partial f}{\partial y}\right)^2}} \right] = \arctan \left[\frac{\frac{\partial f}{\partial t}}{TDX} \right]. \quad (8)$$

Note that the tilt angle measures the dip between the vertical derivative and the magnitude of the horizontal gradient, or TDX , as expressed in equation 4. Combining the concepts of the tilt angle, T , and the magnitude of the horizontal derivative, TDX , Verduzco et al. (2004) introduced the total horizontal derivative of the tilt angle, given by

$$THDR = \sqrt{\left(\frac{\partial T}{\partial x}\right)^2 + \left(\frac{\partial T}{\partial y}\right)^2}. \quad (9)$$

Although the $THDR$ operation looks like a single derivative as expressed in equation 9, it is actually seen to be a second derivative of the original data, when combined with equation 8. Thus, as pointed out by Cooper and Cowan (2008), this operator can enhance the noise of the data if you are not careful with the initial processing.

Wijns et al. (2005) introduced the theta map

$$\cos \theta = \frac{\sqrt{\left(\frac{\partial f}{\partial x}\right)^2 + \left(\frac{\partial f}{\partial y}\right)^2}}{\sqrt{\left(\frac{\partial f}{\partial x}\right)^2 + \left(\frac{\partial f}{\partial y}\right)^2 + \left(\frac{\partial f}{\partial t}\right)^2}}, \quad (10)$$

where $\sqrt{\left(\frac{\partial f}{\partial x}\right)^2 + \left(\frac{\partial f}{\partial y}\right)^2 + \left(\frac{\partial f}{\partial t}\right)^2}$ is called the analytic signal amplitude.

Finally, Cooper and Cowan (2008) introduce the normalized standard deviation ratio of the derivatives, given as

$$NSTD = \frac{\sigma\left(\frac{\partial f}{\partial t}\right)}{\sigma\left(\frac{\partial f}{\partial x}\right) + \sigma\left(\frac{\partial f}{\partial y}\right) + \sigma\left(\frac{\partial f}{\partial t}\right)}. \quad (11)$$

Although this attribute appeared to give good results for potential field data, the results were not very useful when applied to seismic data, so we will focus in the next section on the attributes defined by equations 4 and 8 through 10. That is, we will apply the attributes derived directly from the temporal and spatial derivatives of the data.

REAL DATA EXAMPLE

The data used in this section is a subset of a structurally complex seismic volume over the F3 Block of the Netherlands portion of the North Sea. It has been graciously provided to us by Dr. Paul de Groot of dGB Earth Sciences. As Dr. de Groot stated in a personal email to the first author:

“The F3 data set is released under the Creative Commons License Agreement. That is a license for sharing data and information under similar terms and conditions as open source license agreements like GPL. The essence of the Creative Commons License agreement is that the data can be used for anything that in general terms is considered to be a good thing. Developing new technology and passing on the information fits that category. The data is distributed under the Creative Commons License Agreement <http://creativecommons.org/licenses/by-sa/3.0/> .

Also, this dataset was pre-processed using the Insight Earth® Footprint Removal Workflow, which involved:

1. Structure tensor data analysis involving a volumetric computation of structural strike and dip at each sample in the volume.
2. Iterative footprint removal of five separate wavelength and azimuth orientations.
3. Final 3 inline x 3 crossline x 1 sample median filter.

The result of this workflow was a dataset that showed very little imprint of the acquisition footprint, as will be clear from the data examples.

From a geologic perspective, the F3 dataset can be described as follows:

“F3 is a block in the Dutch sector of the North Sea. The block is covered by 3D seismic that was acquired to explore for oil and gas in the Upper-Jurassic–Lower Cretaceous strata, which are found below the interval selected for this demo dataset.

The upper 1200ms of the demo set consists of reflectors belonging to the Miocene, Pliocene, and Pleistocene. The large-scale sigmoidal bedding is readily apparent, and consists of the deposits of a large fluvio-deltaic system that drained large parts of the Baltic Sea region. The deltaic package consists of sand and shale, with an overall high porosity (20–33%). Some carbonate-cemented streaks are present. A number of interesting features can be observed in this package. The most striking feature is the large-scale sigmoidal bedding, with text-book quality downlap, toplap, onlap, and truncation structures (extracted from the dGB OpenDetect training manual)”.

These bedding features are obvious in Figure 5, which shows three-dimensional images from the F3 block seismic volume. In particular, Figure 5a shows the “outside” of the volume, and Figure 5b shows the “inside”, with a time slice cut from the volume at a time of 1300 ms.

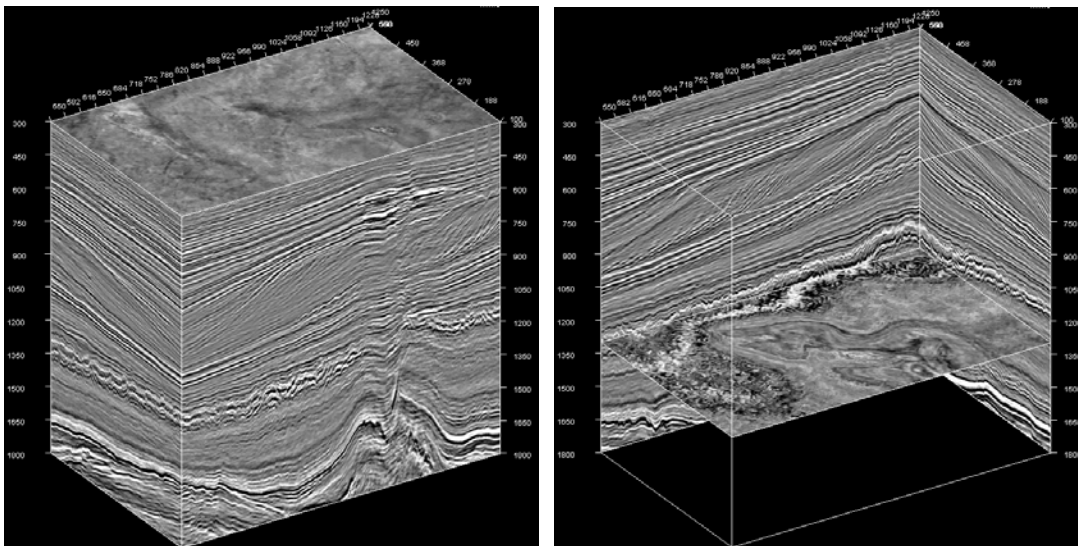


Figure 5: Three-dimensional images of the F3 seismic volume from the North Sea, where (a) shows the “outside” of the volume, and (b) shows the “inside of the volume, with a time slice cut at 1300 ms. Note the very clear structures and bedding present in the seismic volume.

The time slice from 1300 ms has been re-displayed in Figure 6 in map format. We have adopted a grey scale variable density plotting scheme here to better reveal the subtle features of the seismic volume and the attributes that we will be deriving from this volume. Note the small structures on the north and west edges of this slice and the broader structure shown in the centre of the map. This particular time slice was chosen for this combination of different structures, to show the effect of the new edge detection algorithms that we discussed in the previous section.

We will start by applying the total horizontal derivative, or *TDX*, filter to the seismic volume, as given in equation 4. A 1300 ms time slice has been cut from the processed volume and is shown in Figure 7. Note the excellent definition of the small circular structures seen on the north and west edges of the slice, as well as the much clearer definition of the larger structure in the centre of the slice. (The fact that this structure looks like a recently unearthed dinosaur skeleton is just a coincidence but is very amusing!).



Figure 6: A map view of the time slice cut at a time of 1300 ms from the seismic volume shown in Figure 5. Note the variation in structures shown on this slice, from very small to very large.

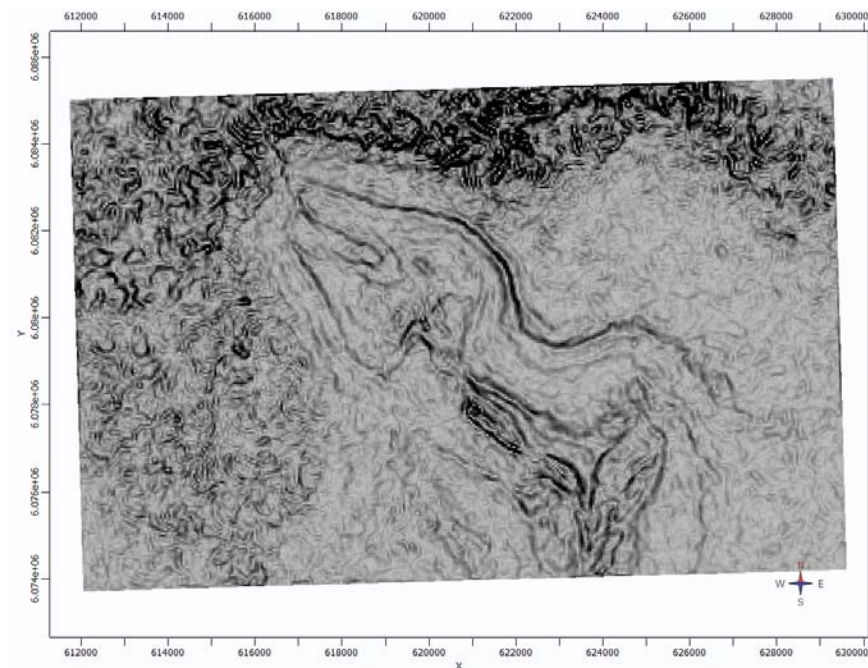


Figure 7: The application of the total horizontal derivative, or *TDX*, filter (equation 4) to the volume shown in Figure 5 and then time sliced at 1300 ms.

Next, we applied the normalized vertical derivative, or tilt angle, filter to the volume shown in Figure 5, and re-sliced the resulting output at a time of 1300 ms. Note that this attribute was computed with equation 8, and is the first attribute that includes the vertical derivative as well as the spatial derivatives. (You will recall that it is computed from the arctangent of the vertical derivative divided by *TDX*.) The result is shown in Figure 8.

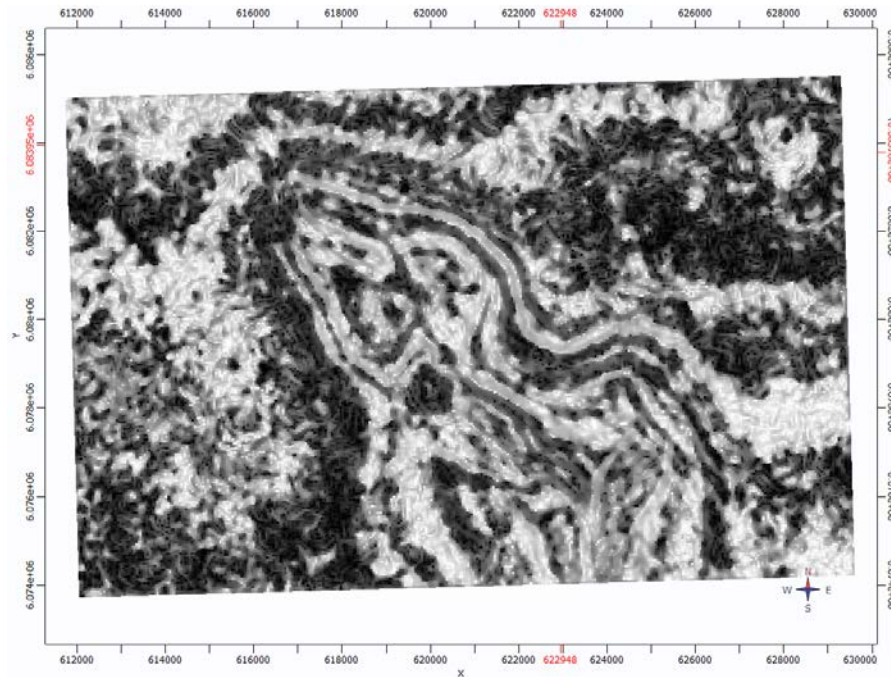


Figure 8: The application of the normalized vertical derivative, or T , filter (equation 8) to the volume shown in Figure 5 and then time sliced at 1300 ms.

The result in Figure 8 clearly shows the structural features of the original data slice, but that these features appear lower frequency than on the TDX plot of Figure 7. Figure 9 then shows the total horizontal derivative of the tilt angle, or $THDR$, filter, which is the application of equation 9.

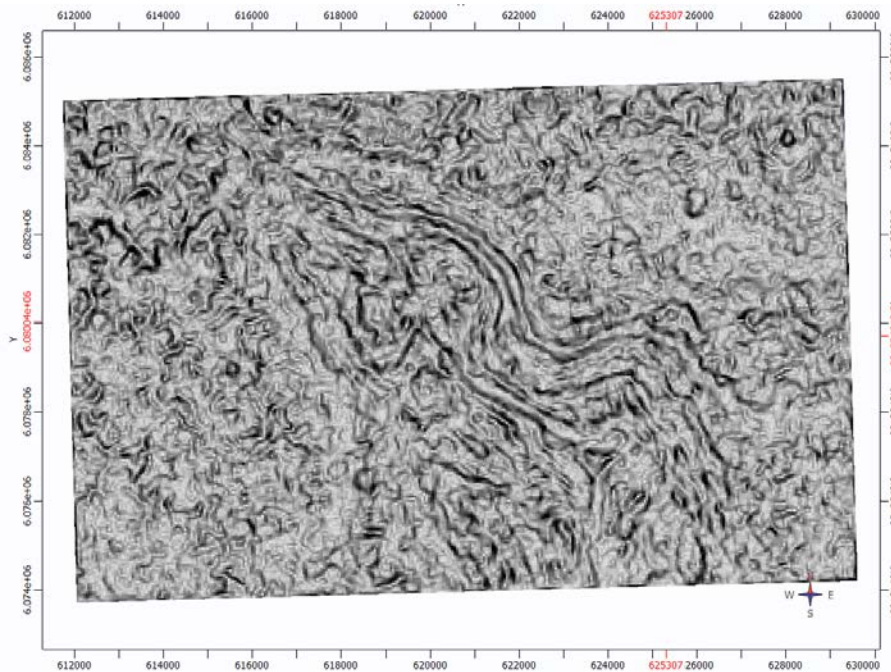


Figure 9: The application of the total horizontal derivative of the tilt angle, or $THDR$, filter (equation 9) to the volume shown in Figure 5 and then time sliced at 1300 ms.

The results of the THDR filter are extremely detailed, and look like we have applied an equalization of all the structures found on the original map slice.

Figure 10 next shows the theta map, computed from equation 10, which shows the structures, but in less detail. Finally, Figure 11 shows the second eigenvalue of the eigen-coherency attribute as a comparison to all the previous maps.

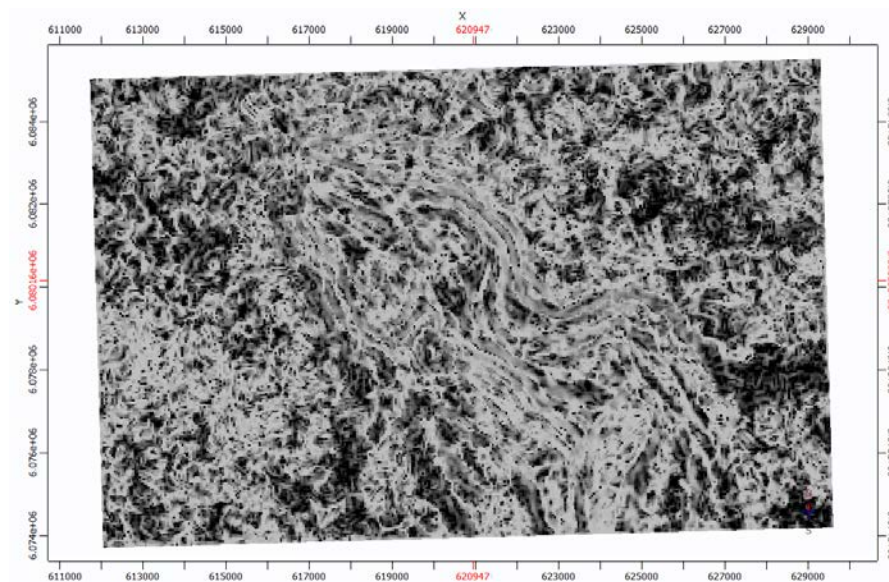


Figure 10: The application of the theta map (equation 10) to the volume shown in Figure 5 and then time sliced at 1300 ms.

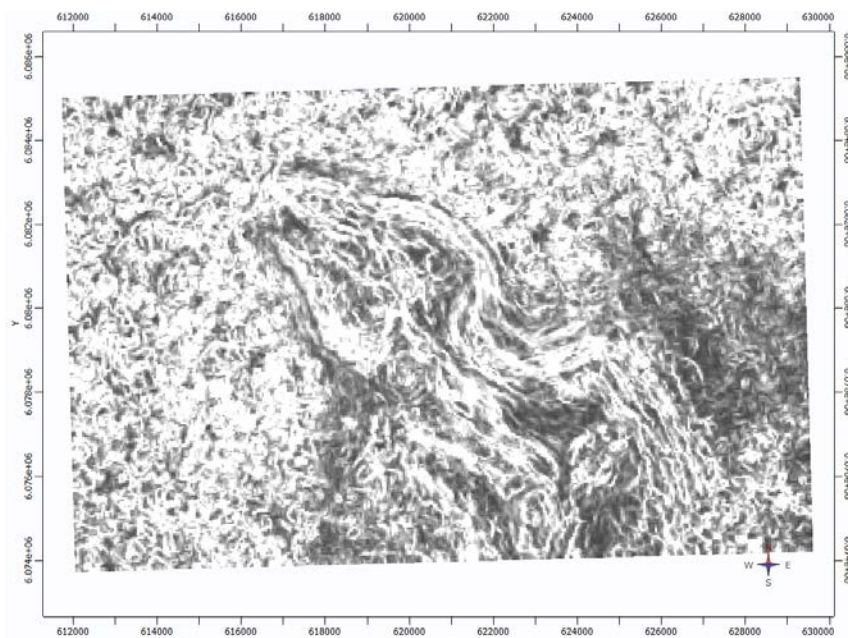


Figure 11: The application of the eigen-coherency method to the volume shown in Figure 5 and then time sliced at 1300 ms.

Note that the result in Figure 11 is less detailed than some of the other methods we have shown. Since there are many “flavours” of the coherency algorithm, the result in Figure 11 could be different for different implementations of coherency. However, coherency does purport to show the same types of discontinuous features as the other methods described here, so it should be comparable to the other figures.

As a final summary, Figure 12 shows a comparison of the input data, the coherency result, and the TDX and THDR results. Each map, including the seismic slice itself, shows the basic structures, and each has its own advantages. For example, the seismic slice (Figure 12a) clearly shows the large folds in the centre of the map and the smaller circular structures on the edges. The eigen-coherency result (Figure 12b) is the least detailed of the four plots but shows the main structures reasonably clearly, including some details in the east part of the map that are not visible on the other plots. The total horizontal derivative, or *TDX*, filter slice (Figure 12c) clearly shows the outlines of both the main folds and the smaller folds to the north and west. The total horizontal derivative of the tilt angle, or *THDR*, filter slice (Figure 12d) is the most detailed of all of the slices, and shows all the features in a much more balanced way than the other plots.

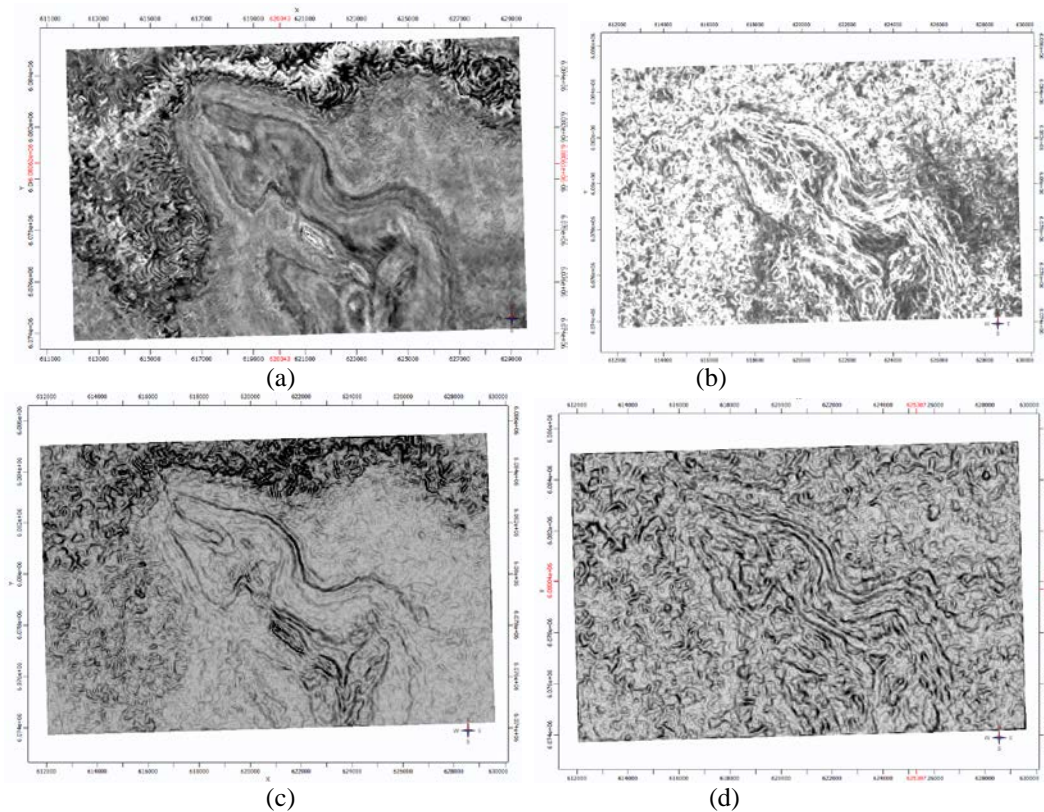


Figure 12: A summary of the various time slices cut at 1300 ms, where (a) shows the input seismic data slice, (b) shows the eigen-coherency slice, (c) shows the total horizontal derivative, or *TDX*, filter slice, and (d) shows the total horizontal derivative of the tilt angle, or *THDR*, filter slice.

CONCLUSIONS

In this article we presented an overview of a number of new options for edge detection on seismic volumes. The edge detection methods for seismic interpretation discussed here all involve derivatives of the seismic volume in the time, inline and cross-line directions. The methods discussed were adapted from techniques that were initially applied to potential field data for edge enhancement, and are similar to algorithms that have already been proposed for seismic edge detection, which involve spatial differences between traces. As discussed, the edge detection methods discussed here were also very similar to coherency and semblance-based methods for seismic discontinuity detection, which in their initial form were based on cross-correlations between traces rather than derivatives.

After a discussion of the mathematics of each attribute transform, the methods were illustrated by a time slice from a structurally complex seismic volume recorded in the North Sea. As was discussed in the final section, each approach had its own advantages and disadvantages. The seismic slice at 1300 ms, deep in the structurally complex part of the volume, clearly showed the large folds in the centre of the map and the smaller circular structures on the edges. The total horizontal derivative, or *TDX*, filter slice clearly showed the outlines of both the main folds and the smaller folds on the data slice to the north and west. The total horizontal derivative of the tilt angle, or *THDR*, filter slice produced the most detailed results of all of the slices, and displayed all the features in a much more balanced way than the other results. The coherency result, which was produced as a comparison to these new methods, was the least detailed of the results but still showed the main structures reasonably clearly. In addition, it displayed some details in the east part of the map that were not visible on the other display.

In summary, the new edge detection algorithms in this study, which were adapted to seismic data from their initial use in potential field data, show a lot of promise for the delineation of structures in seismic data volumes. When compared to the coherency method, which is considered one of the main approaches to fault delineation, these new methods behaved extremely well.

REFERENCES

- al-Dossary, S., Marfurt K.J., and al-Binhassan, N., 2003, Comparative Study of Edge Detection Algorithms: SEG Technical Program Expanded Abstracts.
- al-Dossary, S., and Marfurt, K. J., 2006, 3D volumetric multispectral estimates of reflector curvature and rotation: *Geophysics*, **71**, 41–51.
- Bahorich, M. S., and S. L. Farmer, 1995, 3-D seismic discontinuity for faults and stratigraphic features, The coherence cube: *The Leading Edge*, **16**, 1053–1058.
- Barnes, A. E., 1996, Theory of two-dimensional complex seismic trace analysis: *Geophysics*, **61**, 264–272.

Canny, J., 1986, A computational approach to edge detection: IEEE Transactions on Pattern Analysis and Machine Intelligence, 8, 679-698.

Chopra, S. and K.J. Marfurt, 2012, Which curvature is right for you? Part 2: Presented at the 2012 CSPG/CSEG/CWLS GeoConvention.

Cooper, G.R.J. and Cowan, D.R., 2008, Edge enhancement of potential-field data using normalized statistics: Geophysics, **73**, no. 2, H1-H4.

Gabor, D., 1946, Theory of communication, part I: J. Int. Elect. Eng., v. 93, part III, p. 429-441.

Gersztenkorn, A., and K. J. Marfurt, 1999, Eigenstructure based coherence computations as an aid to 3D structural and stratigraphic mapping: Geophysics, **64**, 1468-1479.

Gonzalez, R.C., and Woods, R.E., 2008, Digital Image Processing: Pearson Prentice Hall, Upper Saddle River, New Jersey.

Luo, Y., Higgs, W. G. and Kowalik, W.S., 1996, Edge detection and stratigraphic analysis using 3D seismic data: SEG Technical Program Expanded Abstracts.

Marfurt, K. J., 2006, Robust estimates of 3D reflector dip: Geophysics, 71, 29-40.

Marfurt, K. J., R. L. Kirlin, S. H. Farmer, and M. S. Bahorich, 1998, 3D seismic attributes using a running window semblance-based algorithm: Geophysics, **63**, 1150-1165.

Miller, H. G., and V. Singh, 1994, Potential field tilt — A new concept for location of potential field sources: Journal of Applied Geophysics, **32**, 213-217.

Russell, B., 2012, Dennis Gabor: The father of seismic attribute analysis, CREWES Research Report.

Taner, M. T., F. Koehler, and R. E. Sheriff, 1979, Complex seismic trace analysis: Geophysics, **44**, 1041-1063.

Torreao, J.R.A. and Amaral, M.S., 2002, Signal differentiation through a Torreao and Amaral's function approach: Pattern Recognition Letters, 23, 1755-1759.

Verduzco, B., J. D. Fairhead, C. M. Green, and C. MacKenzie, 2004, The meter reader—New insights into magnetic derivatives for structural mapping: The Leading Edge, **23**, 116-119.

Wijns, C., C. Perez, and P. Kowalczyk, 2005, Theta map: Edge detection in magnetic data: Geophysics, **70**, no. 4, L39-L43.